scientific reports

Check for updates

OPEN

# Sub-terahertz near field channel measurements and analysis with beamforming and Bessel beams

Duschia Bodet[1]✉, Vitaly Petrov[2], Sergey Petrushkevich[1] & Josep M. Jornet[1]

**Sub-terahertz communications (100–300 GHz) are explored today as a candidate technology to enable extremely high-rate, low-latency data services and high-resolution sensing in beyond-fifth-generation (beyond-5G) wireless networks. However, these sub-terahertz wireless systems will often have to operate in the near field, where the signal propagation does not follow canonical far-field models, including the commonly used free space path loss equation. Instead, the signal propagation in the near field follows more complex patterns that are not well-captured with analytical far-field models standardized for 5G research. Moreover, state-of-the-art beamforming solutions exploited heavily in fourth-generation (4G) and 5G networks are notably less efficient in the near field. In this article, the near-field sub-terahertz channel is accurately measured and analyzed. In addition to state-of-the-art beamforming, the article also analyzes the sub-terahertz channel measurements when using near-field-specific Bessel beams that demonstrate fewer power fluctuations in the near field in addition to higher focusing gain. Novel distance-centric and angle-centric dependencies reported in this article may serve as a reference when developing next-generation channel models for sixth-generation (6G) and beyond-6G near-field sub-terahertz wireless systems.**

While the standardization process for the fifth-generation (5G) wireless networks is coming to its end in a few years with the 3GPP work on New Radio (NR) Release 19 already started in 2024 and NR Release 20 expected to be the last 5G-Advanced release, the research community is slowly shifting its focus toward beyond-5G wireless technologies[1–4]. Despite controversial commercial results for first deployments of 5G-grade millimeter-wave radio (mmWave, 30–71 GHz) and the recent desire to unlock extensive spectrum in "mid bands" (7–24 GHz) for data exchange, it is almost inevitable that next-generation networks (either within the sixth-generation, 6G, or beyond-6G timeline) will eventually also harness higher frequencies laying in the sub-terahertz (sub-THz) band between 100 and 300 GHz[5,6]. High-frequency and ultra-broadband sub-THz wireless systems are particularly identified as a candidate enabler for extremely high-rate, low-latency, and high-reliability 6G and beyond-6G services, as well as high-resolution wireless network sensing[7–12].

The principal difference between state-of-the-art 5G-grade mmWave systems and beyond-5G sub-THz wireless communications is the fact that the latter will often have to operate in the near field[3]. While the entire research and development area on near-field communications is not fundamentally new[13], applying state-of-the-art knowledge to ultra-broadband, extremely directional, and high-rate sub-THz systems faces severe challenges. Specifically, the relatively large physical size of sub-THz antennas together with the short wavelength make the near-field zone around the transmitter antenna non-negligible. The actual length will vary substantially depending on the use case and setup, but following a canonical Fraunhofer distance equation (the boundary between the near-field and far-field regions)[14] it becomes evident that the sub-THz near-field zone may easily expand over several tens of meters ultimately reaching a few hundreds of meters in extreme configurations[3,15]. Hence, several prospective use cases for sub-THz wireless communications, including high-rate wireless local area networks (WLANs) and small cells, will have to often operate in the near field[16]. It has been recently mathematically proven that any ultra-broadband *mobile* sub-THz wireless network will always have at least a few users in the near field[17].

[1]Department of Electrical and Computer Engineering and Institute for the Wireless Internet of Things, Northeastern University, Boston, MA 02115, USA. [2]Division of Communications Systems, School of Electrical Engineering and Computer Science, KTH Royal Institute of Technology, 114 28 Stockholm, Sweden. ✉email: bodet.d@northeastern.edu

In this sub-THz near-field zone, the phase difference between the components of the electromagnetic (EM) wave arriving at different parts of the receiver antenna is non-negligible anymore, hence contradicting the plane wave assumption. The plane wave assumption in turn is a basis for widely-utilized far-field propagation models, including the common free space path loss (FSPL) model following a closed-form equation by Friis from 1946[18]. In contrast, near-field sub-THz channels feature complex and non-monotonic behavior, where the average received power may even increase with the spreading distance in certain cases that strictly contradicts the far-field Friis law[3,19,20]. *Accurately and comprehensively characterizing the sub-THz propagation in the near field is one of the essential steps toward harnessing these attractive bands in 6G and beyond-6G wireless systems*[3,15].

Another key novel concept for sub-THz near-field propagation is related to the *wavefront engineering*—the process of adjusting the amplitude and phase profile of the EM wave to propagate in a certain way. In the near field, non-planar wave propagation provides additional flexibility in designing beams[20]. Conventional state-of-the-art beamforming solutions result in Gaussian beams, but in the near-field, the set of possible design options also includes beamfocusing (sometimes referred to as "near-field beamforming")[16,21], curved-shape Airy beams[22], and Bessel beams[23,24], among other options. Recently, THz and sub-THz Bessel beams have attracted particular interest due to their non-diffracting nature (focusing a substantial part of the energy alongside a fixed-length straight vector segment in the near field[20,24]), as well as their self-healing properties which allow them to overcome partial signal blockage[10,25]. A variety of recent works have characterized the propagation of THz or sub-THz Bessel beams generated using polytetrafluorethelene axicons[26], 3-D printed diffractive axicons[27], and even a plasmonic beamforming technology[28]. Pulsed THz Bessel beams have also been explored for their potential in communications and sensing[29,30]. Particularly, the self-healing property of Bessel beams is of high importance for high-rate low-latency high-reliability services in 6G and beyond, including eXtended Reality (XR) and the Metaverse, as frequent blockage of sub-THz links by stationary and mobile obstacles may compromise stringent latency and reliability quality of service (QoS) constrains[31–33].

Over the recent decades, THz and sub-THz communication channels have been studied in various use cases, from next-generation indoor wireless networks[34,35] down to wireless-networks-on-chip (WNoC) on one end[36] and up to sub-THz satellite links on the other[37]. These primarily include extensive modeling efforts with dozens of channel and propagation models reported to date[8,38]. However, the overwhelming majority of these sub-THz and THz channel models are built with the far-field assumption in mind, so are not fully applicable to characterize complex propagation in the sub-THz near field. To date, only a very limited fraction of sub-THz channel models account for near-field propagation effects, primarily either related to the near-field sensing[39,40], focused on the near-field propagation in the human body[41–43], or, recently, modeling sub-THz multiple-antenna systems in the near field as a superposition of several far-field systems[44–47].

As the observed near-field sub-THz channel features complex non-monotonic propagation, it is desired to have reliable reference measurements in the sub-THz near-field to verify existing and future channel models for 6G and beyond-6G sub-THz high-rate communication systems. The majority of available measurement-based studies on sub-THz communication channels are however also far-field, by design[35,48–51], as further reflected in the latest surveys and tutorials on the topic[8,38]. Complementing the far-field-centric measurement studies above, some recent works made attempts to empirically characterize the near-field sub-THz communication channel. Among others, J. Fu et al.[52] illustrated the effect of separation distance for several frequencies and compared the results with their developed model. Further, Y. Wang et al.[53] compared the path gain and the phase change across the far field and the near field using a virtual antenna array. There are a few other empirical studies available, however, the overwhelming majority of measurement-based works for near-field communications are focused on lower frequencies in the microwave and mmWave bands[54–56]. *Hence, to the best of the authors' knowledge, the set of available reference measurements for near-field sub-THz communications covering all the key dimensions together (distance, angle, frequency, and beam type/wavefront) is limited to date.*

Motivated by the continuously growing interest in near-field sub-THz communications on one side and the limited availability of reliable comprehensive channel measurements for near-field sub-THz links on the other, we attempt to close this gap in the current article. *In this work, experimental results and their analysis are provided for near-field propagation in sub-THz 6G and beyond wireless communications. Specifically, four key dependencies are explored together related to the effect of distance, the effect of offset angle, the effect of frequency, and the effect of the utilized sub-THz beam.* For the latter, a direct comparison between a conventional Gaussian beam (produced e.g., as a result of 5G-grade beamforming)[14,57–59] and a non-diffracting sub-THz Bessel beam (further described in Methods)[23,24] is provided. Our study particularly indicates a notable difference in the system characteristics with the Gaussian beam and with the Bessel beam thus confirming the importance of accounting for the transmitted signal's beam type when operating in the sub-THz near field. On top of specific observations and conclusions made in the article, the work also provides illustrative measurement data that can be used as a reference when developing near-field-specific 6G and beyond-6G channel models for sub-THz wireless communication systems.

## Results

In this study, four major near-field-specific propagation effects are explored for sub-THz communications. The first is the effect of the separation distance between the transmitting and receiving antennas. The second is the effect of the offset angle of the transmitting antenna from 0 degrees (corresponding to perfect alignment between the transmitting and receiving antennas). Here, the obtained results illustrate the non-trivial differences between the antenna radiation diagram at various distances within the near field and the well-established radiation diagram of the same antenna in the far field. Third, we also illustrate how the change in the sub-THz frequency impacts the propagation characteristics when both the separation distance and the offset angle stay the same. Finally, the fourth key effect explored is the effect of the type of beam utilized for communications. Specifically, the last subsection presents a comparison between the results with a Gaussian beam (often the resulting type

when utilizing far-field beamforming[14]) and a non-diffracting sub-THz Bessel beam (suggested recently for near-field wireless systems)[20,25].

## Effects of separation distance and frequency in the sub-THz near field for a Gaussian beam

The impact of the transmission distance on the received power in the near field is shown in Fig. 1. Each panel displays the received power in dBm for a linear sweep performed using the Gaussian beam at a different range of distances within the sub-THz near field. The solid lines are the measured results, and the dashed lines show what the expected received power would be according to the far-field Friis path loss equation[18]:

$$P_{rx} = G_{tx} + G_{rx} + P_{tx} + 20\log\left(\frac{\lambda}{4\pi d}\right), \tag{1}$$

where $G_{tx}$ and $G_{rx}$ are the gains of the transmit and receive antennas respectively, $P_{tx}$ is the transmit power in dBm, $\lambda$ is the signal wavelength and $d$ is the transmission distance.

There are several key observations from the results in Fig. 1. First, comparing the measured power in the near field with the expected power based on the Friis equation, we see up to a 30 dB difference in Fig. 1a. As expected, the Friis path loss expression does not accurately characterize the loss experienced in the near field. In Fig. 1b (3–3.5 m away from the transmitter), the difference between the expected power following the far-field model and the measured power is around 4–10 dB, which is still a major mismatch. Further, in Fig. 1c the difference continues decreasing down to 3–6 dB. Hence, at a 6 m distance, the real measured power in the sub-THz near field is from two to four times lower than what the conventional far-field model predicts. As we would expect, as the separation distance increases and the far-field boundary is approached, the measured results get closer to the well-known trend for far-field propagation. Still, for a wide range of practical distances (e.g., 3 m to 6.5 m), the difference is substantial and should be accounted for in the design of next-generation sub-THz communication systems. It is also clear, however, that determining how to compensate for the difference between the Friis equation and the measured results is not particularly straightforward. Changing the exponential in the Friis equation would change the slope of the curve, but would not introduce the fluctuations we are observing. Similarly, adding a multiplicative factor would shift the curve up or down, but not solve for the fundamental trend that is vastly different from that given by Friis.

Analyzing the effect of frequency, we see a common trend across all three distance regions presented in Fig. 1. Specifically, the system utilizing a greater frequency experiences greater loss at a given fixed distance. For far-field model curves shown with the dashed lines, the difference between 120 and 160 GHz stays the same across all the distances (around ≈2.5 dB). Meanwhile, the difference between the measured results for 120 GHz and 160 GHz varies across distances due to the non-monotonic nature of the power vs. distance dependency in the near field. Furthermore, this difference is, on average, around 1 dB larger than the corresponding difference between the far-field curves. The latter is partially explained by the Fraunhofer distance[14], $d_F = \frac{2D^2}{\lambda}$, where $D$ is the largest dimension of the antenna aperture and $\lambda$ is the signal wavelength. Accordingly, the distance to the near-field boundary increases with frequency. For example, the Fraunhofer distance for 120 GHz is about 11 m and almost 15 m for 160 GHz. We also observe that the measured near-field curves in Fig. 1 (especially, Fig. 1c) approach the far-field trend slower with distance. Therefore, as the theoretical near-field to the far-field boundary is farther away at a higher frequency, we see minor additional losses there.

We proceed with our analysis of the non-monotonic behavior of power vs. distance dependency in the sub-THz near field in Fig. 2. This figure presents a subset of the measurement results from Fig. 1, for illustration purposes focusing only on the lowest and the highest measured frequencies: 120 GHz and 160 GHz. For each of the curves, the measurement results are complemented by both the sliding average (across 40 nearest measurements with 1 mm step, so within a 0.04 m "window") as well as a label including the average peak-to-peak

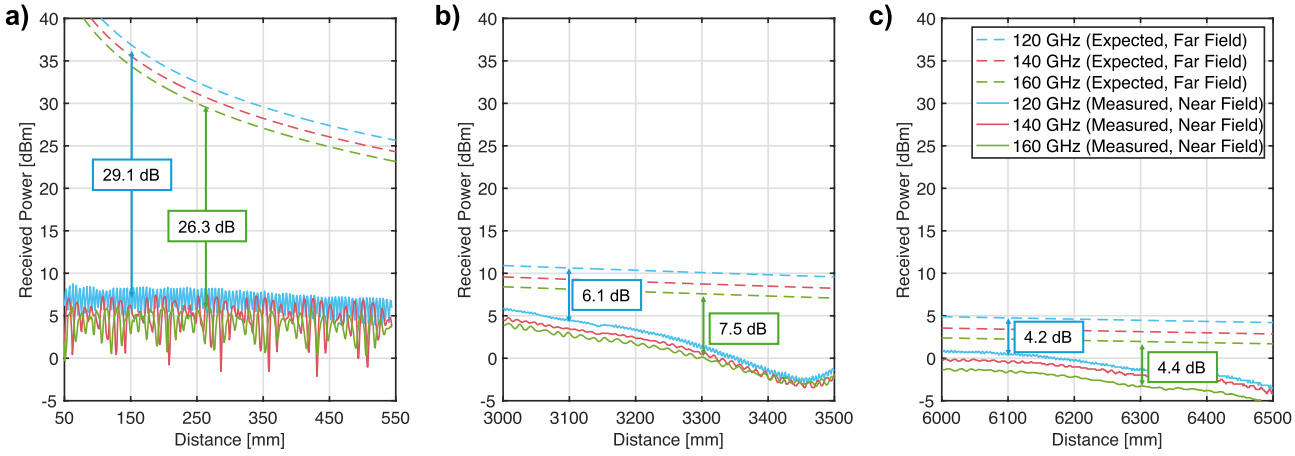


**Fig. 1.** Effects of distance and frequency for the sub-THz Gaussian beam. Measured received power as a function of separation distance. Three panels representing illustrative distance ranges in the sub-THz near field—(**a**) from 5 to 55 cm, (**b**) from 300 to 350 cm, and (**c**) from 600 to 650 cm.

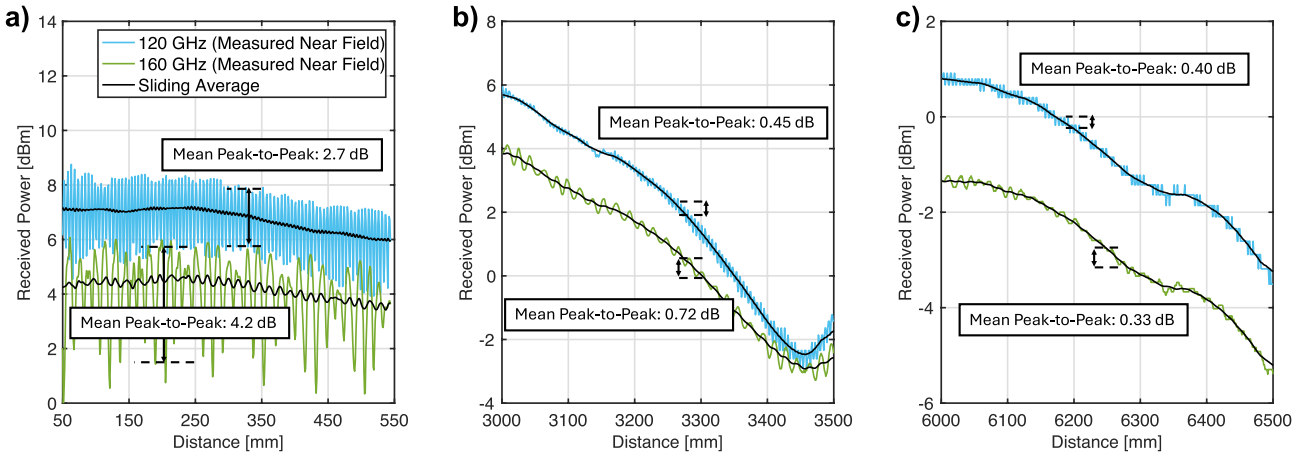


**Fig. 2.** Non-monotonic effects of separation distance in the near field for the sub-THz Gaussian beam. Measured received power as a function of separation distance for 120 GHz and 160 GHz complemented with the sliding averages and the average peak-to-peak value labeled for each panel and frequency. Three panels representing illustrative distance ranges in the sub-THz near field—(**a**) from 5 to 55 cm, (**b**) from 300 to 350 cm, and (**c**) from 600 to 650 cm.

power over the measurement results of that panel. In Fig. 2 we specifically observe two types of oscillations in the measurement results over distance: (i) rapid oscillations over distances of a few millimeters, and (ii) slower oscillations over several centimeters (visible from the sliding average curves). Both types are still present in Fig. 2b but are weaker in amplitude and almost disappear at distances greater than 6 m, as visible from Fig. 2c.

In Fig. 2a, the rapid oscillations' peak-to-peak values are 2.7 dB and 4.2 dB for 120 GHz and 160 GHz respectively. By the 6 m mark, we see they have dropped to 0.40 dB and 0.33 dB in Fig. 2c. The slower oscillations are most clearly seen in the sliding average for 120 GHz in Fig. 2a, but in Fig. 2b, both 120 GHz and 160 GHz observe a considerable trough at 3460 mm. Even in Fig. 2c, in which both signals follow a downward trend, the trend is not consistent.

To further illustrate these findings, we plot the probability density functions (PDFs) for each measurement in Fig. 3 (as in real deployment the exact separation distance between the transmitter and the receiver may be not known with 1 mm precision). Each column corresponds to a different range of transmission distances (0.05–0.55 m, 3–3.5 m, and 6–6.5 m), while each row corresponds to a different frequency measured. For all frequencies, we see the center value of the PDF migrating to the left (i.e. to smaller values) as the transmission distance increases. This trend corresponds to the fact that, in general, as the transmission distance increases the received power decreases.

We also notice that for the 0.05 m to 0.55 m range, there is typically one peak value in the PDF, while for both the 3 m to 3.5 m range and the 6 m to 6.5 m measurements, there are multiple (usually, two) peak values within each PDF. Hence, the PDFs for shorter distances reflect unimodal distribution, while other measurements tend to follow the multimodal distribution (specifically, bimodal in most cases). This difference in distribution is partially due to the fact that at longer distances, fast oscillations presented in Fig. 2a decrease in amplitude,

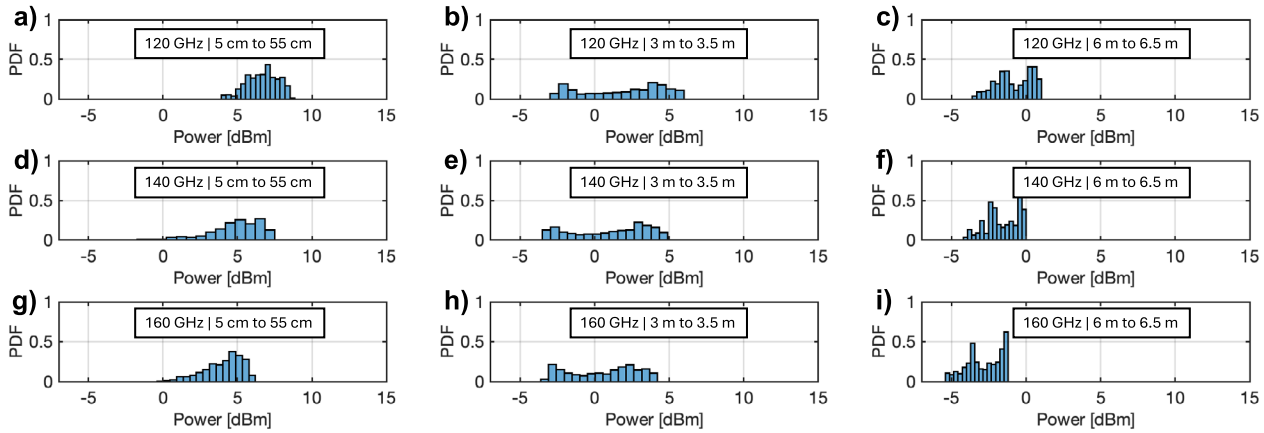


**Fig. 3.** Probability Density Function (PDF) of measured received power for various frequencies and separation distance ranges—(**a**–**c**) Results at each range of distances for 120 GHz, (**d**–**f**) Results at each range of distances for 140 GHz, (**e**–**h**) Results at each range of distances for 160 GHz.

so the slower trends start dominating. An illustrative example here is in Fig. 2c, where the 100 GHz curve has two quasi-stable segments: the first one around 4 dBm between 6000 and 6100 mm and the second one around 2 dBm between 6300 and 6400 mm. These two peaks of values are well reflected in Fig. 3c and similar trends are observed for other frequencies and distances.

We finally cross-verify the findings from Figs. 1, 2 and 3 with 4, that reports the standard deviation (STD) of the results presented in Fig. 3. The standard deviation is indicated in dBm for each frequency over the three measured cases. As observed from Fig. 4, the standard deviation trends constantly downward as the transmission distance increases, and almost constantly downward with frequency as well which corresponds to the major findings reported above.

## Effect of offset angle and impact of distance on the antenna radiation pattern in the sub-THz near field

As the key effects of the separation distance and the frequency are revealed in Figs. 1, 2, 3 and 4, we proceed with our analysis by studying the implications of the alignment/misalignment between the transmitting and receiving antennas in Fig. 5.

Specifically, Fig. 5a illustrates the radiation pattern of the transmitting antenna observed in the sub-THz near field at different distances. To obtain the values reported in Fig. 5, we subtracted the known spreading loss in the power spectral density over a given fixed distance from the difference between the known transmit power and the measured received power. The resulting value in dB was then divided by two, as the setup for Gaussian beam measurements utilizes two identical horn+lens antennas, as further discussed in Methods below. We complemented the measured antenna radiation pattern in Fig. 5a,b with the far-field radiation diagram of the same antenna taken from its specification[60].

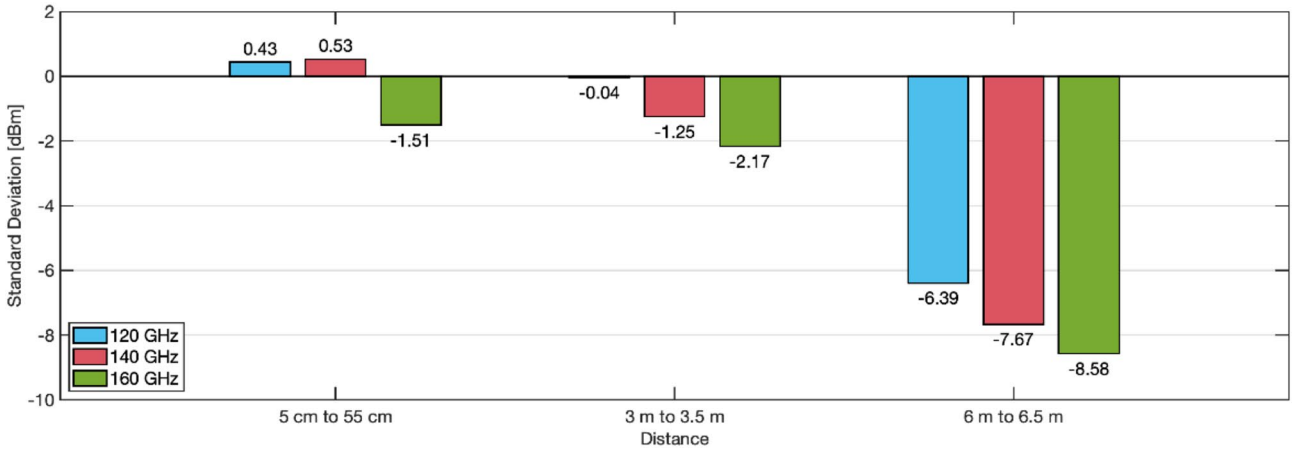


**Fig. 4.** Standard deviation (STD) of the measured received power results. STD calculated over the entirety of each of the three measurement sets presented in Fig. 1a–c.

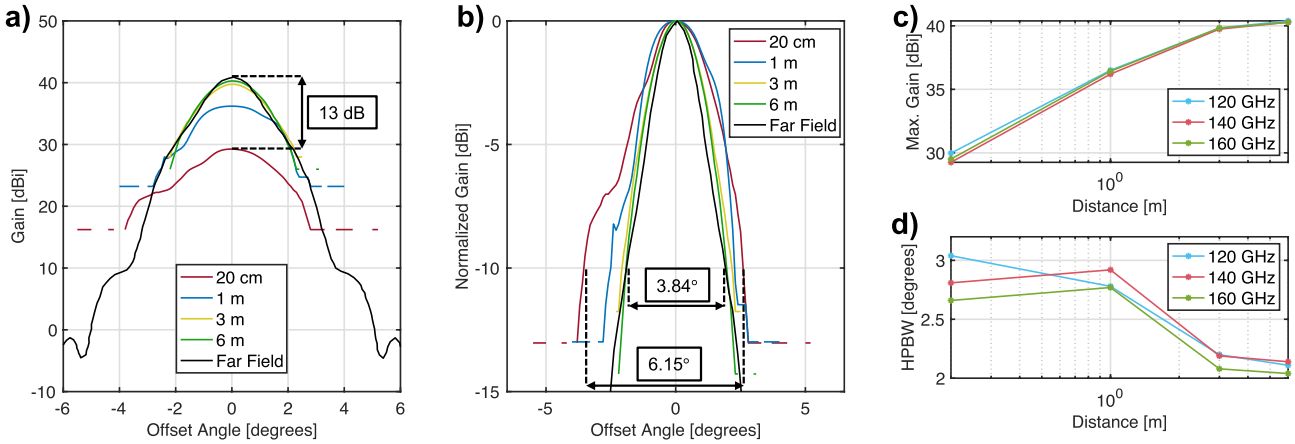


**Fig. 5.** Effect of the offset angle. Measured angular sweep results—(**a**) Gain at each measurement distance and the expected far-field gain from the antenna specifications[60] at 140 GHz, (**b**) Normalized gain at each measurement distance and expected normalized far-field gain at 140 GHz, (**c**) Maximum (max.) gain observed at each distance for all the measured frequencies, (**d**) Half Power Beam Width (HPBW) of the antenna radiation pattern observed at each distance for all measured frequencies.

Exploring Fig. 5a, we observe that the maximum gain increases with the separation distance. Specifically, the difference between the observed maximum gain for the 20 cm distance and the reported maximum gain for this antenna in the far field is around 13 dB. This deviation from the far-field maximum gain decreases with distance (6 dB, 3 dB, and 2 dB for the results measured at 1 m, 3 m, and 6 m respectively), rapidly for shorter distances and more slowly for longer distances. For example, the 80 cm difference between the red and blue curves corresponds to more than a 5 dB increase in gain while the 3 m difference between the 3 and 6 m measurements results in an increase of less than 1 dB. Thus as the far field approaches, the impact of near-field propagation is less and less apparent but still non-negligible even at distances over 6 m.

It is also important to recall that these results only show the radiation pattern of the antenna at the transmitter. In practice, however, the difference between the real power values in the sub-THz near field and the expected values when following the far-field antenna radiation pattern can be up to two times larger if the sub-THz receiver uses the same directional antenna.

In addition to the increase in maximum gain, as we approach the sub-THz far field, the width of the beam shrinks. This trend is visible in Fig. 5a presenting the real gain but is even easier to see in Fig. 5b where we have normalized the values. For closer distances, the beam is significantly wider than it is for farther distances. We also note a minor asymmetry in the measured results for shorter distances, explained by either an imperfect initial alignment during the measurements (extremely hard to achieve at very short distances) or imperfect manufacturing of the particular antenna sample. Despite these artifacts, the key trends related to frequency, angle, and separation distance still hold across all the reported measurements, as further illustrated in Fig. 5c,d discussed below.

Figure 5c presents the maximum gain observed at each distance for all the measured frequencies, and we observe the steady upward trend for all cases. We also see that the maximum gain is highest for 120 GHz (i.e., the lowest frequency). As mentioned previously, higher frequencies will observe a larger near-field region for the same antenna aperture due to their smaller wavelengths. Thus, the gain for lower frequencies increases faster than for higher frequencies. Finally, in Fig. 5d we present the half-power beamwidth (HPBW) of the measured antenna radiation pattern as a function of distance. Here, we observe that the beamwidth decreases with distance for all frequencies, which cross-verifies our observation regarding the opposite trend in the maximum gain. As the same antenna does not start radiating less or more energy when the receiver is moved to a different distance, the lower maximum gain in the sub-THz near field leads to a wider beam (more energy radiated in other directions), as reported in Fig. 5.

## Effect of beam type: comparing Gaussian beam and Bessel beam results in the sub-THz near field

We conclude the presentation of key results with Fig. 6, which compares the distance-related and angle-related dependencies of propagation for conventional Gaussian beams (similar to what a far-field beamforming system would produce) with near-field-specific non-diffracting sub-THz Bessel beams. For illustration purposes, the Gaussian beam measurement results are plotted with dashed lines. The Bessel beam measurement results compensated for the different antennas used at the receiver are plotted with dotted lines, while the Bessel beam results also compensated for the absorption loss of the axicon are shown with solid lines. The non-diffracting region of the Bessel beam (between 50 and 250 mm) is clearly visible in Fig. 6a where we plot the received power in dBm as a function of the transmission distance.

We observe from Fig. 6a that the Bessel beam adds up to a 6.4 dB gain compared to the Gaussian. We still see slight oscillations in the received power of the Bessel beam along its non-diffracting region, but these fluctuations are significantly smaller in amplitude than those experienced by the Gaussian beam. Hence, in the sub-THz near field, the use of the Bessel beam instead of the conventional Gaussian beam allows not only for

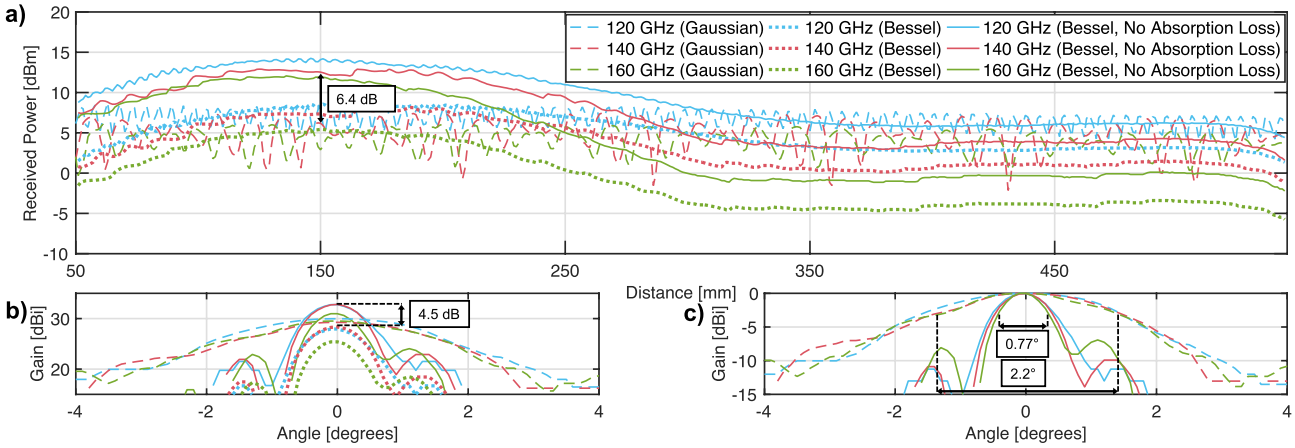


**Fig. 6.** Effect of the sub-THz beam. Comparing the sub-THz Gaussian beam with the sub-THz Bessel beam in the near field—(**a**) Received power as a function of distance for the Gaussian and Bessel beams showing results with and without compensating for the absorption of axicon's material, (**b**) Antenna gain for the Gaussian and the Bessel beams, (**c**) Normalized gain as a function of offset angle for the Gaussian and the Bessel beams.

greater received power but also for more stable received power at various distances. The latter may be important for next-generation mobile sub-THz communications in the near field toward 6G and beyond.

Further, in Fig. 6b we plot the observed gain for the Bessel beam and Gaussian beam at 20 cm for different offset angles. One notable difference is the gain. There is a 4.5 dB difference in maximum gain between the Bessel and Gaussian performance. Beyond this increase, however, we also see what appear to be side lobes at plus and minus 1.3 degrees, which correspond to the first ring of the Bessel beam's amplitude profile[24]. These are more clearly visible in Fig. 6c where we present the normalized gain for both the Gaussian and Bessel beams. The characteristically narrower focus of the Bessel beam is also apparent in this plot: the HPBW of the Bessel is narrower by over 1 degree, which is a notable improvement for a narrow-beam ≈40 dBi antenna with the HPBW of only a few degrees in the far field.

We finally note that the non-diffracting region of the sub-THz Bessel beam is not theoretically limited to 30 cm, which may be too short for many practical 6G communication use cases. Similarly, the gain of the Bessel beam is not strictly limited to 6.4 dB. These values are due to the properties of a particular 3D-printed axicon used to generate the Bessel beam in our measurements, as further detailed in Methods. Meanwhile, different configurations of the axicon are possible, as well as different approaches to generate the Bessel beam using conventional phased arrays or intelligent reflective surfaces (IRSs)[20].

## Discussion

The above results present important insights into the sub-THz communication channel characteristics in the near field as a function of all key parameters, including the distance between the transmitter and receiver, the offset angle between the antennas, the selected frequency, and the utilized beam type (specifically, illustrated by Gaussian vs. Bessel beams).

*First*, it has been confirmed (as also observed in prior studies) that using the canonical monotonic far-field FSPL expression for near-field sub-THz communications leads to substantial errors. Specifically, as seen in Fig. 1, the measured near-field results are up to 30 dB off from the FSPL prediction. This finding emphasizes the need for some alternative expression for the near field. Although we can resort to Maxwell's equations when the far-field path loss equations are invalid, ideally, there should be an alternative of lower computational complexity but with acceptable accuracy.

Fortunately, the findings in this paper suggest that it may be possible to find such an expression leveraging the reported measurement results. As previously discussed, the distance-dependent results illustrate three primary trends: (i) a gradual decrease in power as the distance increases, (ii) slow oscillations of the sliding average, and (iii) fast fluctuations in the measured values especially for shorter ranges. Follow-up studies may explore if these three phenomena can be characterized together in a simple expression, similar to existing far-field channel models that account for fast and slow fading in addition to the FSPL.

*Second*, as observed in Fig. 5, the radiation pattern of the sub-THz antenna in the near field is notably different from the one it features in the far field (both in terms of maximum gain and beam width). Moreover, the far-field specific antenna radiation pattern typically reported in the antenna specifications becomes less and less valid when decreasing the separation distance between the sub-THz transmitter and receiver.

Practically, aside from impacting the received power at the receiver, the increase in HPBW as the transmission distance decreases could affect the physical layer security (enabling eavesdroppers at wider angles), interference (sending greater power to other nodes around), and beam training (as the beams may be wider than anticipated at certain distances). Thus, these aspects must be accounted for when designing sub-THz communication systems and networks. Specifically, both the analytical models and the engineering solutions that rely on the antenna's directivity for sub-THz systems should become aware of whether or not these systems are in the near field and how the radiation pattern is impacted accordingly.

*Third*, beyond characterizing the propagation of traditional Gaussian beams, our results also indicate the promise of non-diffracting beams (specifically, Bessel beams) for future sub-THz communications, given higher gains with these beams in the near field and their notably more focused radiation patterns. Although we used an axicon lens to generate the Bessel beams for this experiment, just like Gaussian beams, Bessel beams can also be created using antenna arrays. Such sub-THz arrays can dynamically adjust the parameters and phase profile to provide a longer or shorter depth of focus in addition to tighter or wider focal lines. The exploration and eventual utilization of razor-sharp sub-THz Bessel beams open the door to novel system design options and new performance boundaries to be achieved with near-field sub-THz communications in 6G and beyond-6G wireless networks. Specifically, Bessel beams present a viable solution to the severe fluctuations we observe in Figs. 1 and 2. Given their non-diffracting nature in the near field and the presented results, they are a promising alternative.

*In conclusion*, the sub-THz near field is an integral part of the beyond-5G beyond wireless connectivity landscape, and an empirical study on near-field sub-THz communication channel behavior has been provided. This study highlights the key dependencies crucial for future system design choices and may serve as a reference for next-generation channel models capturing the near-field propagation of (beyond-)6G sub-THz communications.

## Methods

The measurement campaign was carried out in two stages. The distance-related results reported in Figs. 1, 2, 3, 4 and 6a have been obtained by the authors in the sub-THz lab at the U. S. Air Force Research Laboratory (AFRL) in Rome, NY, USA, as further detailed in "Linear Sweep" subsection below and illustrated in Fig. 7a. The second part of the measurements revealing the angular-related dependencies reported in Fig. 5, 6b,c has been performed at Northeastern University in Boston, MA, USA, as further described in the "Angular Sweep" subsection below and illustrated in Fig. 7b. For consistency, both measurement setups utilized the same sub-THz

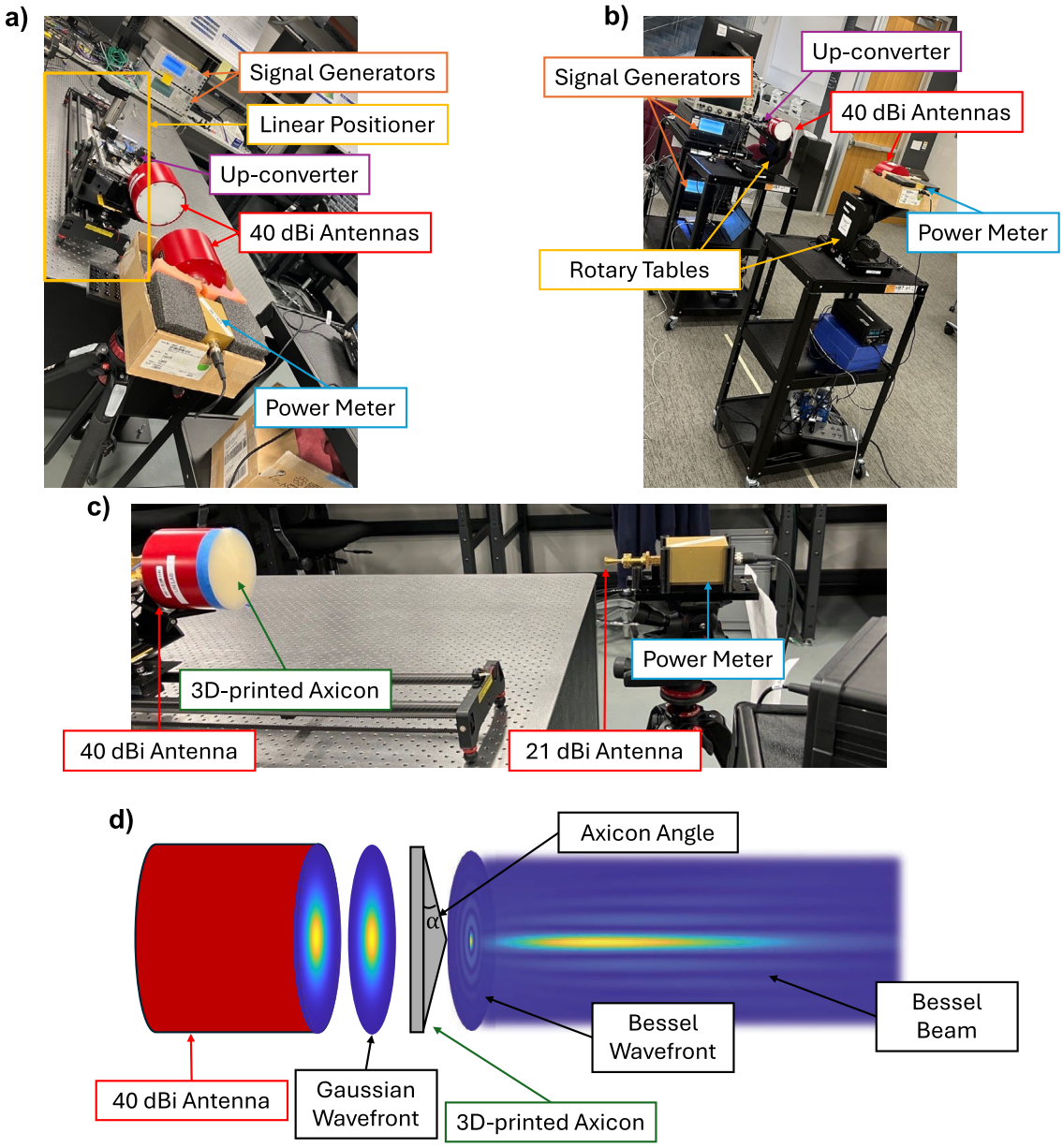


**Fig. 7.** Experimental setup—(**a**) Experimental platform with the programmable linear track at the Air Force Research Laboratory (AFRL), (**b**) Experimental platform with programmable rotary tables at Northeastern University, (**c**) Experimental set-up for the Bessel beam linear measurement using the 3-D printed axicon (angle-related measurements used the similar approach to generate the Bessel beam), (**d**) Illustration of the 3D axicon transforming the incoming sub-THz Gaussian beam into the sub-THz Bessel beam.

radio equipment and configurations, as discussed in the following subsection. The key parameters for our study are also summarized in Table 1.

## Sub-THz signal transmission and reception

To generate sub-THz signals we used an up-converter chain (Virginia Diodes) with a design frequency of 130 GHz, as illustrated in Fig. 7a,b. The up-converter passes a local oscillator (LO) signal through two frequency doublers before mixing the LO signal with a provided intermediate frequency (IF) signal. The resulting radio frequency (RF) signal is amplified by a power amplifier and radiated from the transmitter antenna. We used two signal generators (Keysight Performance Signal Generators). One to supply an IF signal of 1 GHz, and the other to supply LO signals of 27.75 GHz, 34.75 GHz, and 39.75 GHz to correspond to RF signals of 120 GHz, 140 GHz, and 160 GHz. We used an ethernet connection to control the signal generators from a laptop during experiments. At the receiver side, the signal was captured by another sub-THz antenna connected to a power meter (Virginia Diodes PM5) through a waveguide. For the Gaussian beam case (beamforming), two identical horn antennas equipped with a focusing lens were used (Anteral HGLHA-40-WR06): one antenna at the transmitter and one at the receiver. The up-converter and antennas are frequency-selective and impart different gains at each frequency

| Category | Parameter | | Linear Sweep | Angular Sweep |
|---|---|---|---|---|
| Setup | Transmitter-Receiver distance | | 0.05–0.5 5m,<br>3–3.5 m,<br>6–6.5 m | 0.2 m, 1 m,<br>3 m, 6 m |
| | Sweep resolution | | 1mm | 0.1 degrees |
| | Transmitter antenna offset angle | | 0 degrees<br>(perfect alignment) | [-10 degrees,<br>10 degrees] |
| Radio | IF power | | 0 dBm | |
| | LO power | | 10 dBm | |
| | RF power after up-converters | | ≈12 dBm | |
| | Frequency | | 120 GHz, 140 GHz, 160 GHz | |
| Transmitter Antenna | Gaussian and Bessel Beam | Type | Horn + lens (Fig. 7A) | |
| | | Model | Anteral HGLHA-40-WR06 | |
| | | Dimensions | 118 mm | |
| | | Max gain | 40 dBi | |
| Receiver Antenna | Gaussian Beam | Type | Horn + lens (Fig. 7A) | |
| | | Model | Anteral HGLHA-40-WR06 | |
| | | Dimensions | 118 mm | |
| | | Max gain | 40 dBi | |
| | Bessel Beam | Type | Horn | |
| | | Model | VDI WR-6.5 | |
| | | Dimensions | 10.8 mm | |
| | | Max gain | 21 dBi | |
| Bessel beam axion | Axicon angle | | 10 degrees | |
| | Axicon Diameter | | 118 mm | |
| | Depth of Focus | | 250 mm | |
| | Maximum Depth of Axicon | | 16.4 mm | |
| | Minimum Depth of Axicon | | 6 mm | |

**Table 1.** Key parameters of the conducted measurement study.

measured[61]. To determine the compensation factors for this, we measured the output power of the up-converter without the antennas and consulted the specifications of the antennas used[60].

When measuring the sub-THz Bessel beam propagation in the near field, the same horn+lens antenna was used at the transmitter side with a 3D-printed axicon secured in front of the antenna system to convert the wavefront from that of a Gaussian beam to that of a Bessel beam[24,25]. More details concerning the axicon itself are detailed in the corresponding subsection below and illustrated in Fig. 7c. At the receiver side, we used a horn antenna (VDI WR-6.5)[62] without a focusing lens to avoid changing the form of the Bessel beam (by sending it through a lens) before measuring the power. We measured the gain of this horn antenna as a function of frequency and found it to be 21.5, 20, 21.5 for 120 GHz, 140 GHz, and 160 GHz respectively. When comparing the results of the Gaussian and Bessel beams we use a frequency and distance-dependent correction factor to account for the change in effective gain between the horn (VDI) and the horn+lens (Anteral) antennas. This compensation factor considers the distance-dependent difference in gain between the VDI horn antenna, which is operating within its far-field region, and the Anteral horn+lens antenna, which has the near-field distance-dependent response shown in Fig. 1. Thus, the received data provided in Fig. 6 is adjusted according to the frequency response of the transmitter front-end as well as the frequency and distance-dependent difference in gain between the VDI horn antenna and the Anteral horn+lens antenna. Meanwhile, the "No Absorption Loss" data has been further adjusted to compensate for the absorption loss introduced by the axicon. We provide more details on this compensation process in the sub-section on *Sub-THz Bessel beam generation and reception* below.

## Linear sweep

To explore the effect of the separation distance between the transmitter antenna and the receiver antenna in the sub-THz near field, a set of measurements has been collected at various separation distances. To achieve the greatest precision, we utilized a *programmable linear positioning slide* (see Fig. 7a) available at the U.S. AFRL radio lab in Rome, NY, USA. The device has a linear range of 95 cm and 1 mm resolution. The linear slide was controlled by an Arduino board, connected via a cable to a computer running the MATLAB code to orchestrate the experiment and store the measured data.

We started with mounting the sub-THz transmitter on this positioning slide and the sub-THz receiver (antenna connected to the power meter) on a tripod, as illustrated in Fig. 7a. Then, the transmitter and the receiver were manually aligned for all illustrative starting distances (0.55 m, 3.5 m, and 6 m) in the sub-THz near field. This process involved adjusting the angle of the linear positioning system with the up-converter and the position of the tripod holding the power meter such that the maximum power was observed by the power

meter at the receiver side. We then did a few preliminary sweeps prior to each actual measurement to ensure that the system remained aligned as the transmitter moved along the track.

For the actual measurement results reported above, we: (i) sequentially sent sinusoidal signals at each sub-THz RF frequency; (ii) recorded the power observed in each case (each of the frequencies and each distance); and then moved the transmitter antenna forward by 1 mm, thus decreasing the separation distance between the transmitter and the receiver antennas. Following this procedure, three distance ranges were measured with 1 mm spatial resolution: (i) from 0.05 m to 0.55 m; (ii) from 3 m to 3.5 m; and (iii) from 6 m to 6.5 m, as illustrated in Figs. 1, 2, 3, 4 and 6a in the Results section above.

## Angular sweep

In addition to the distance-dependent behavior, in this work, we also explored how much the radiation pattern of a sub-THz antenna changes between the far field (where the overwhelming majority of antennas are typically characterized today) and the near field (where, as detailed in the Introduction, many prospective sub-THz communication and sensing use cases will operate in practice in 6G and beyond networks in future).

The angular sweep experiments were conducted by placing the transmitter and the receiver (power meter) on two dual-axis *programmable computer-controlled rotary tables* (IntelLiDrives), as illustrated in Fig. 7b. These tables use a worm gear drive design combined with stepper motors to enable precise angular positioning down to 0.0005 degrees. On both the transmitter and the receiver sides, the rotary table orientation (and thus the antenna orientation as well) was controlled by a computer running the experiment. For this purpose, both transmitter and receiver rotary table stepper motors were connected to a laptop via a Recommended Standard 232 (RS-232) to Universal Serial Bus (USB) cable. The MATLAB code to run the experiment then utilized an in-house built C++ library to control the rotation tables remotely over the USB interface.

The actual measurements reported in the Results section above (specifically, Figs. 5, 6b,c) started with accurately setting a given separation distance between the transmitter and the receiver sub-THz antennas. Then, the preliminary alignment of the antennas has been done manually by sending the needed rotation commands to both rotary tables involved. Later, a search algorithm was run on both the transmitter and the receiver sides to find the orientation of the transmitter and receiver antennas leading to their best possible alignment. Here, as the measured setup represents a line-of-sight link (no obstacles on the way and no strong reflections), the maximum received power was used as the criterion for the alignment.

Once the alignment configuration was found, a horizontal angular sweep was performed at the transmitter side to rotate the transmitter antenna with steps of 0.1 degrees, while recording the average received power level at the receiver (power meter) for every angular configuration. Thus the measurement involved, (i) sequentially sending sinusoidal signals at each sub-THz frequency of interest, (ii) storing the observed power at each frequency, and (iii) rotating the transmitter 0.1 degrees to the next position. This process was repeated until the entire angular range from -10 degrees to +10 degrees was covered. Finally, the entire set (separation distance verification, alignment, and four angular sweeps, one per frequency) was repeated for another distance between the transmitter and the receiver. As a result, three sub-THz frequencies (120 GHz, 140 GHz, and 160 GHz) have been characterized for each of the four distances, leading to sixteen measurement sets reported in Fig. 5.

## Sub-THz Bessel beam generation and reception

As a final stage for both distance sweep and angular sweep measurement parts, a comparison has been performed between the commonly used Gaussian beam (e.g., from a horn antenna or as a result of beamforming with an antenna array) and one of the candidate near-field non-diffracting beams for sub-THz systems—Bessel beam[15]. Unlike the Gaussian beam wavefront in Fig. 7d which features a bright spot in the center that radially decreases in intensity when spreading, the Bessel beam wavefront (also shown in Fig. 7d) has a tight focus surrounded by concentric rings. Each of these rings carries part of the signal power, and together they enable the non-diffracting and self-healing properties of the Bessel beams[23–25].

To generate the sub-THz Bessel beam, we utilized a 3D-printed axicon mounted securely to the transmitter antenna (after the lens), as illustrated in Fig. 7c. This axicon is a rotationally symmetric prism acting as a secondary lens for the transmitted signal. The primary design parameters for an axicon are the refractive index of its material, the size of the lens and the incident beam, and the axicon angle, depicted in Fig. 7d. The radius of the incident beam and the axicon angle together dictate the Bessel beam's depth of focus, which is around 30 cm for this experiment. The axicon is created from Polylactic acid, also called PLA, with a maximum and minimum thickness of 1.64 cm and 0.6 cm, respectively, using a commercial 3D printer (Ultimaker 3)[25]. We measured the absorption coefficient of PLA at 120 GHz, 140 GHz, and 160 GHz to be 1.17 $cm^{-1}$, 1.08 $cm^{-1}$, and 1.35 $cm^{-1}$ respectively. The geometry of the axicon is designed to enable gains greater than the losses of the medium as indicated by the presented results.

The major difference in the setup for the Gaussian beam and for Bessel beam transmissions (in both linear and angular sweeps) is the sub-THz antenna used at the receiver side. While Gaussian beam measurements utilized identical sub-THz antennas (horn + lens) at the transmitter and receiver as illustrated in Fig. 7a,b, the measurements with Bessel beams used the same (horn + lens) antenna at the transmitter, but a simple horn antenna (without the lens) at the receiver as shown in Fig. 7c. The rationale for this change is not to corrupt the sub-THz Bessel beam (generated by a sequence of horn, lens, and an additional 3D-printed axicon, as in Fig. 7c) before it reaches the receiver.

## Post-processing the results for sub-THz Bessel beam

The "Bessel, No Absorption Loss" results in Fig. 6 demonstrate what the received power would be assuming (i) that the same gain antenna is used at the power meter as in the Gaussian beam case, and (ii) that the Bessel

beam is generated without any loss due to the material of the axicon. This additional set of curves is introduced to account for the fact that sub-THz Bessel beams can be generated using various methods that would not all have identical losses[63,64]. Hence, we complement the results achieved in our given measurement study with the results achievable in a similar setup but featuring a zero-loss generation of sub-THz Bessel beams, which serves as an upper bound for the sub-THz Bessel beam performance in the considered scenario.

To determine the received power curves in Fig. 6a, the following expressions are used. The "Bessel, No Absorption Loss" values are given by

$$P_{rx,Lossless}(f,d) = P_{rx,measured}(f,d) + G_{NF,Anteral}(f,d) - G_{VDI}(f) + L_{axicon}(f,d), \tag{2/}$$

while the "Bessel" data, accounting for the difference in receiver antenna, is calculated according to

$$P_{rx}(f,d) = P_{rx,measured}(f,d) + G_{NF,Anteral}(f,d) - G_{VDI}(f). \tag{3}$$

$P_{rx,measured}(f,d)$ is the received power as a function of frequency and distance, $G_{NF,Anteral}(f,d)$ and $G_{VDI}(f)$ are the near-field gain of the Anteral antenna and far-field gain of the VDI antenna respectively, and $L_{axicon}(f,d)$ is the absorption loss of the axicon. $G_{NF,Anteral}(f,d)$ is given by:

$$G_{NF,Anteral}(f,d) = \frac{P_{rx,Gaussian}(f,d) - P_{rx,FSPL}(f,d) + 2G_{FF,Anteral}(f)}{2}, \tag{4}$$

where $P_{rx,Gaussian}(f,d)$ is the measured power using both Anteral antennas, $P_{rx,FSPL}(f,d)$ is the anticipated power according to FSPL (both shown in Fig. 1), and $G_{FF,Anteral}(f)$ is the far-field gain of the Anteral antennas. Using knowledge of the geometry and the refractive index of the axicon[65], $L_{axicon}(f,d)$, the absorption loss introduced by the axicon material as a function of distance, is calculated:

$$L_{axicon}(f,d) = e^{\beta(f)(0.006+|w_0-r_a(d)|\tan(\alpha))}. \tag{5}$$

As stated in Table 1, $0.006m$ is the minimum thickness of the axicon. In other words, the entirety of the beam travels through $0.006m$ of material before any other delay and phase shift is introduced. $\beta$ is the frequency-dependent absorption loss of PLA, $w_0$ is the radius of the axicon illuminated by the Anteral antenna, $\alpha$ is the axicon angle, and $r_a(d)$ is given by:

$$r_a(d) = min\left(\frac{d - w_0\tan(\alpha)}{\frac{1}{\tan(\alpha)} - \tan(\alpha)}, w_0\right). \tag{6}$$

Hence, these additional "Bessel, No Absorption Loss" results complement the measurement data in Fig. 6, covering a more general case. Specifically, these additional curves characterize the estimated behavior of sub-THz Bessel beams if they get generated by a lossless approach not involving any axicons[63,64].

## Data availibility

All data can be made available to readers upon reasonable request to the corresponding author.

Received: 1 March 2024; Accepted: 16 August 2024
Published online: 24 August 2024

## References

1. Dang, S., Amin, O., Shihada, B. & Alouini, M.-S. What should 6G be?. *Nat. Electron.* **3**, 20–29 (2020).
2. Chen, W. *et al.* 5G-advanced toward 6G: Past, present, and future. *IEEE J. Sel. Areas Commun.* **41**, 1592–1619 (2023).
3. Cui, M., Wu, Z., Lu, Y., Wei, X. & Dai, L. Near-field MIMO communications for 6G: Fundamentals, challenges, potentials, and future directions. *IEEE Commun. Mag.* **61**, 40–46 (2022).
4. Alwis, C. D. *et al.* Survey on 6G frontiers: Trends, applications, requirements, technologies and future research. *IEEE Open J. Commun. Soc.* **2**, 836–886 (2021).
5. Nokia. Nokia's vision for the 6G era. *White Paper* (2022).
6. Samsung. 6G. The next hyper-connected experience for all. The vision on 6G. *White Paper* (2020).
7. Rappaport, T. S. *et al.* Wireless communications and applications above 100 GHz: Opportunities and challenges for 6G and beyond. *IEEE Access* **7**, 78729–78757 (2019).
8. Han, C. *et al.* Terahertz wireless channels: A holistic survey on measurement, modeling, and analysis. *IEEE Commun. Surv. Tutor.* **24**, 1670–1707 (2022).
9. Giordani, M., Polese, M., Mezzavilla, M., Rangan, S. & Zorzi, M. Toward 6G networks: Use cases and technologies. *IEEE Commun. Mag.* **58**, 55–61 (2020).
10. Petrov, V., Guerboukha, H., Mittleman, D. M. & Singh, A. Wavefront hopping: An enabler for reliable and secure near field terahertz communications in 6G and beyond. *IEEE Wirel. Commun.* **31**, 48–55 (2024).
11. Al-Daffaie, S., Jumaah, A. J., Rubio, V. L. & Kusserow, T. Design and implementation of a terahertz lens-antenna for a photonic integrated circuits based THz systems. *Sci. Rep.* **12**, 1476 (2022).
12. Jornet, J. M., Knightly, E. W. & Mittleman, D. M. Wireless communications sensing and security above 100 GHz. *Nat. Commun.* **14**, 841 (2023).
13. Coskun, V., Ozdenizci, B. & Ok, K. A survey on near field communication (NFC) technology. *Wirel. Pers. Commun.* **71**, 2259–2294 (2013).
14. Balanis, C. A. *Antenna Theory: Analysis and Design* (Wiley, 2015).
15. Petrov, V., Bodet, D. & Singh, A. Mobile near-field terahertz communications for 6G and 7G networks: Research challenges. *Front. Commun. Netw.* **4**, 1151324 (2023).
16. Zhang, H., Shlezinger, N., Guidi, F., Dardari, D. & Eldar, Y. C. 6G wireless communications: From far-field beam steering to near-field beam focusing. *IEEE Commun. Mag.* **61**, 72–77 (2023).

17. Petrov, V., Jornet, J. M. & Singh, A. Near-field 6G networks: Why mobile terahertz communications MUST operate in the near field. In *Proc. of the IEEE Global Communications Conference (GLOBECOM)*, 1–7 (2023).
18. Friis, H. T. A note on a simple transmission formula. *Proc. IRE* **34**, 254–256 (1946).
19. Bjornson, E. & Sanguinetti, L. Power scaling laws and near-field behaviors of massive MIMO and intelligent reflecting surfaces. *IEEE Open J. Commun. Soc.* **1**, 1306–1324 (2020).
20. Singh, A. *et al.* Wavefront engineering: Realizing efficient terahertz band communications in 6G and beyond. *IEEE Wireless Communications* 1–7 (2023).
21. Bjornson, E. *et al.* Towards 6G MIMO: Massive spatial multiplexing, dense arrays, and interplay between electromagnetics and processing (2024). arXiv: 2401.02844.
22. Liu, C., Niu, L., Wang, K. & Liu, J. 3D-printed diffractive elements induced accelerating terahertz Airy beam. *Opt. Express* **24**, 29342–29348 (2016).
23. Durnin, J., Miceli, J. J. & Eberly, J. H. Diffraction-free beams. *Phys. Rev. Lett.* **58**, 1499–1501 (1987).
24. Lloyd, J., Wang, K., Barkan, A. & Mittleman, D. M. Characterization of apparent superluminal effects in the focus of an axicon lens using terahertz time-domain spectroscopy. *Opt. Commun.* **219**, 289–294 (2003).
25. Reddy, I. V. *et al.* Ultrabroadband terahertz-band communications with self-healing bessel beams. *Commun. Eng.* **2**, 70 (2023).
26. Wu, Z. *et al.* Vector characterization of zero-order terahertz bessel beams with linear and circular polarizations. *Sci. Rep.* **7**, 13929 (2017).
27. Niu, L. *et al.* Diffractive elements for zero-order bessel beam generation with application in the terahertz reflection imaging. *IEEE Photon. J.* **11**, 1–12 (2018).
28. Monnai, Y., Jahn, D., Withayachumnankul, W., Koch, M. & Shinoda, H. Terahertz plasmonic bessel beamformer. *Appl. Phys. Lett.***106** (2015).
29. Bitman, A., Moshe, I. & Zalevsky, Z. Improving depth-of field in broadband thz beams using nondiffractive bessel beams. *Opt. Lett.* **37**, 4164–4166 (2012).
30. Kulya, M. S., Semenova, V. A., Bespalov, V. G. & Petrov, N. V. On terahertz pulsed broadband gauss-bessel beam free-space propagation. *Sci. Rep.* **8**, 1390 (2018).
31. Wang, G. *et al.* Development of metaverse for intelligent healthcare. *Nat. Mach. Intell.* **4**, 922–929 (2022).
32. Aslam, A. M. *et al.* Metaverse for 6G and beyond: The next revolution and deployment challenges. *IEEE Internet of Things Mag.* **6**, 32–39 (2023).
33. Khoshkholghi, M. A. *et al.* xURLLC in 6G with meshed RAN. *ITU J. Fut. Evol. Technol.* **3**, 612–622 (2022).
34. Priebe, S. & Kurner, T. Stochastic modeling of THz indoor radio channels. *IEEE Trans. Wirel. Commun.* **12**, 4445–4455 (2013).
35. Ju, S., Xing, Y., Kanhere, O. & Rappaport, T. S. Millimeter wave and sub-terahertz spatial statistical channel model for an indoor office building. *IEEE J. Sel. Areas Commun.* **39**, 1561–1575 (2021).
36. Timoneda, X., Cabellos-Aparicio, A., Manessis, D., Alarcon, E. & Abadal, S. Channel characterization for chip-scale wireless communications within computing packages. In *2018 Twelfth IEEE/ACM International Symposium on Networks-on-Chip (NOCS)*, 1–8 (2018).
37. Kokkoniemi, J., Jornet, J. M., Petrov, V., Koucheryavy, Y. & Juntti, M. Channel modeling and performance analysis of airplane-satellite terahertz band communications. *IEEE Trans. Veh. Technol.* **70**, 2047–2061 (2021).
38. Liu, S., Yu, X., Guo, R., Tang, Y. & Zhao, Z. THz channel modeling: Consolidating the road to THz communications. *China Commun.* **18**, 33–49 (2021).
39. Budiarto, E., Pu, N.-W., Jeong, S. & Bokor, J. Near-field propagation of terahertz pulses from a large-aperture antenna. *Opt. Lett.* **23**, 213–215 (1998).
40. Gürtler, A., Winnewisser, C., Helm, H. & Jepsen, P. U. Terahertz pulse propagation in the near field and the far field. *JOSA A* **17**, 74–83 (2000).
41. Särestöniemi, M., Pomalaza-Raez, C., Sayrafian, K., Myllylä, T. & Iinatti, J. A preliminary study of RF propagation for high data rate brain telemetry. In *EAI International Conference on Body Area Networks*, 126–138 (2021).
42. Manoufali, M., Bialkowski, K., Mobashsher, A. T., Mohammed, B. & Abbosh, A. In situ near-field path loss and data communication link for brain implantable medical devices using software-defined radio. *IEEE Trans. Antennas Propag.* **68**, 6787–6799 (2020).
43. Jornet, J. M. & Akyildiz, I. F. Channel modeling and capacity analysis for electromagnetic wireless nanonetworks in the terahertz band. *IEEE Trans. Wireless Commun.* **10**, 3211–3221 (2011).
44. Tarboush, S. *et al.* TeraMIMO: A channel simulator for wideband ultra-massive MIMO terahertz communications. *IEEE Trans. Veh. Technol.* **70**, 12325–12341 (2021).
45. Chen, Y. & Han, C. Deep CNN-based spherical-wave channel estimation for terahertz ultra-massive MIMO systems. In *Proc. of the IEEE Global Communications Conference (GLOBECOM)*, 1–6 (2020).
46. Chen, Y., Yan, L. & Han, C. Hybrid spherical-and planar-wave modeling and DCNN-powered estimation of terahertz ultra-massive MIMO channels. *IEEE Trans. Commun.* **69**, 7063–7076 (2021).
47. Maletic, N. *et al.* A study of los mimo for short-range sub-thz wireless links. In *Mobile Communication-Technologies and Applications; 25th ITG-Symposium*, 1–6 (VDE, 2021).
48. Xu, H. *et al.* Virtual antenna array based wideband thz mimo channel measurement. In *2021 IEEE MTT-S International Microwave Workshop Series on Advanced Materials and Processes for RF and THz Applications (IMWS-AMP)*, 222–224 (IEEE, 2021).
49. Priebe, S., Kannicht, M., Jacob, M. & Kürner, T. Ultra broadband indoor channel measurements and calibrated ray tracing propagation modeling at THz frequencies. *J. Commun. Netw.* **15**, 547–558 (2013).
50. Rey, S., Eckhardt, J. M., Peng, B., Guan, K. & Kürner, T. Channel sounding techniques for applications in thz communications: A first correlation based channel sounder for ultra-wideband dynamic channel measurements at 300 ghz. In *2017 9th international congress on ultra modern telecommunications and control systems and workshops (ICUMT)*, 449–453 (IEEE, 2017).
51. Bodet, D. *et al.* Characterizing sub-THz MIMO channels in practice: A novel channel sounder with absolute time reference. In *Proc. of the IEEE Global Communications Conference (GLOBECOM)* (2023).
52. Fu, J., Juyal, P. & Zajić, A. Near field modeling for THz wireless channel in nettop size metal enclosures. In *Proc. of the 15th European Conference on Antennas and Propagation (EuCAP)*, 1–5 (2021).
53. Wang, Y., Sun, S. & Han, C. Far- and near-field channel measurements and characterization in the terahertz band using a virtual antenna array (2024). arXiv:2312.12964.
54. Yuan, Z. *et al.* On phase mode selection in the frequency-invariant beamformer for near-field mmWave channel characterization. *IEEE Trans. Antennas Propag.* **71**, 8975–8986 (2023).
55. Payami, S. & Tufvesson, F. Channel measurements and analysis for very large array systems at 2.6 GHz. In *Proc. of the 6th European Conference on Antennas and Propagation (EuCAP)*, 433–437 (2012).
56. Martinez, A. O., De Carvalho, E. & Nielsen, J. O. Towards very large aperture massive MIMO: A measurement based study. In *Proc. of the IEEE Globecom Workshops (GC Wkshps)*, 281–286 (2014).
57. He, X., Cui, Y. & Tentzeris, M. M. Tile-based massively scalable MIMO and phased arrays for 5G/B5G-enabled smart skins and reconfigurable intelligent surfaces. *Sci. Rep.* **12**, 2741 (2022).
58. Pérez Santacruz, J. *et al.* Outdoor mm-wave 5G/6G transmission with adaptive analog beamforming and IFoF fronthaul. *Sci. Rep.* **13**, 13945 (2023).
59. Ciuonzo, D., Rossi, P. S. & Dey, S. Massive MIMO channel-aware decision fusion. *IEEE Trans. Signal Process.* **63**, 604–619 (2015).

60. Anteral. High gain lens horn antenna. https://anteral.com/products/antenna-passives/high-gain-lens-horn-antennas-hglha/ (2023).
61. Diodes, V. Custom source performance 125 - 225 GHz. https://www.vadiodes.com/en/products/custom-transmitters (2024).
62. Diodes, V. Nominal horn specifications.
63. Khonina, S. N., Kazanskiy, N. L., Khorin, P. A. & Butt, M. A. Modern types of axicons: New functions and applications. *Sensors* **21**, 6690 (2021).
64. Feng, R. *et al.* Flexible manipulation of bessel-like beams with a reconfigurable metasurface. *Adv. Opt. Mater.* **8**, 2001084 (2020).
65. Khonina, S. N., Kazanskiy, N. L., Karpeev, S. V. & Butt, M. A. Bessel beam: Significance and applications-a progressive review. *Micromachines* **11**, 997 (2020).

## Acknowledgements

Part of the data in Results has been collected at the U.S. Air Force Research Laboratory (AFRL) Communications Laboratory at Innovare Advancement Center in Rome, NY. We would like to acknowledge Mr. Steven Arbogast and Mr. Jacob Hall from AFRL for testbed setup and data collection support. The work has been supported in part by the projects CNS-2011411 and CNS-2225590 by the U.S. National Science Foundation (NSF), as well as the project FA9550-23-1-0254 by the U.S. Air Force Office of Scientific Research (AFOSR).

## Author contributions

D.B. and V.P. formulated experiments. D.B., V.P., and S.P. performed experiments. D.B. analyzed the results. J.J. supervised and directed the project. All the authors contributed to writing the manuscript.

## Competing interests

The authors declare no competing interests.

## Additional information

**Correspondence** and requests for materials should be addressed to D.B.

**Reprints and permissions information** is available at www.nature.com/reprints.

**Publisher's note** Springer Nature remains neutral with regard to jurisdictional claims in published maps and institutional affiliations.